Journal of Materials Chemistry C

PAPER

View Article Online
View Journal | View Issue

Cite this: J. Mater. Chem. C, 2015, 3, 10415

Sb deficiencies control hole transport and boost the thermoelectric performance of p-type $AgSbSe_2$†

Satya N. Guin and Kanishka Biswas*

Received 20th May 2015,
Accepted 15th June 2015

DOI: 10.1039/c5tc01429h

www.rsc.org/MaterialsC

Silver antimony selenide, $AgSbSe_2$, a Te free analogue of $AgSbTe_2$, has been known to show a promising thermoelectric performance when it is doped with monovalent (M^+) and divalent (M^{2+}) cations in the Sb sublattice. Here, we report a significant enhancement of the thermoelectric performance of p-type nonstoichiometric $AgSbSe_2$ through Sb deficiencies. Sb deficiencies markedly increase the carrier concentration in $AgSbSe_2$ without the addition of any foreign dopant, which in turn enhances electrical conductivity in the 300–610 K temperature range. Enhancement in the electrical transport results in a remarkable improvement in the power factor (σS^2) values up to ~6.94 μW cm^{-1} K^{-2} at 610 K in $AgSb_{1-x}Se_2$. Notably, we have achieved a nearly constant σS^2 value of ~6 μW cm^{-1} K^{-2} in the 400–610 K temperature range in Sb deficient samples. Additionally, $AgSbSe_2$ exhibits ultra-low thermal conductivity due to phonon scattering because of bond anharmonicity and a disordered cation sublattice. With superior electronic transport and ultra-low thermal conductivity, a peak ZT value of ~1 at 610 K was achieved for the $AgSb_{0.9925}Se_2$ and $AgSb_{0.99}Se_2$ samples. A maximum thermoelectric conversion efficiency (η_{max}) of ~8% was calculated by considering a virtual thermoelectric module consisting of the present p-type $AgSb_{1-x}Se_2$ and previously reported n-type $AgBiSe_{2-x}Cl_x$, by maintaining a temperature difference of ΔT = 400 K.

1. Introduction

To alleviate the demand for fossil fuels and for a greater understanding of the long-term effects of greenhouse gas emissions, a clean and sustainable energy solution is essential. Generation of electrical energy from waste heat by using thermoelectric generators is one of the clean and efficient ways to solve the future energy problems. The conversion efficiency of a thermoelectric device is proportional to the thermoelectric figure of merit of the material, $ZT = \sigma S^2 T/(\kappa_{el} + \kappa_{lat})$, where σ, S, T, κ_{el} and κ_{lat} are the electrical conductivity, Seebeck coefficient, temperature, electrical thermal conductivity, and lattice thermal conductivity, respectively.[1–6] The requirements for high ZT values are a high Seebeck coefficient, high electrical conductivity and low thermal conductivity in the same material.[1–4] The development of high performance materials are challenging because of the well-known interdependence of σ, S and κ. To date, different strategies have been employed to increase the ZT value of inorganic materials. Tuning of charge carrier and phonon transport in the material are the two important aspects of all the discovered approaches. The carrier transport in materials can be altered significantly by the modification of their electronic structure *via* the introduction of resonance levels,[7,8] band convergence,[9,10] quantum confinement effects,[11,12] and electron energy barrier filtering.[13,14] Lattice thermal conductivity (κ_{lat}) is independent of the electrical transport of the material. Thus, different approaches have been taken to reduce the κ_{lat}. Some of the most successful ways to reduce the κ_{lat} are through solid solution alloying,[15] second phase nanostructuring,[15–18] and the all scale phonon scattering approach.[5] High ZT values can be achieved in single phase compounds by utilizing critical phase transitions[19,20] or intrinsically low thermal conductivity.[6] Complex crystal structures with heavy elements, high lattice anharmonicity and soft resonant bonding can also give rise to significantly low thermal conductivity.[3,21,22]

In the last couple of years, tremendous efforts have been devoted to the development of high performance materials based on earth abundant elements, aside from conventional Te containing PbTe, Bi_2Te_3 and $AgSbTe_2$, due to the toxicity and low abundance of Te. Among the different new materials, Te free I–V–VI_2 (where I = Cu, Ag or alkali metal; V = Sb, Bi; and VI = S, Se) chalcogenides are one of the promising class of materials due to their intrinsic low lattice thermal conductivity.[22–24] The low lattice thermal conductivity occurs due to the presence of soft phonon modes, which arises due to the strong hybridization

New Chemistry Unit, Jawaharlal Nehru Centre for Advanced Scientific Research (JNCASR), Jakkur P.O., Bangalore 560064, India. E-mail: kanishka@jncasr.ac.in

† Electronic supplementary information (ESI) available: Thermal diffusivity and heat capacity (Fig. S1), Lorenz numbers (Fig. S2), electronic thermal conductivity (κ_{ele}) (Fig. S3), heating cooling cycle electrical conductivity (σ) and Seebeck coefficient (S) data for $AgSb_{0.9925}Se_2$ samples (Fig. S4). See DOI: 10.1039/c5tc01429h

and repulsion between the ns^2 lone-pair of the group V cation and the valence p orbital of the group VI anion.[22a] In this class of compounds, $AgSbSe_2$, $AgBiSe_2$ and $AgBiS_2$ are known for their promising thermoelectric performance.[20,22,24–28] Among these compounds, $AgSbSe_2$, an intrinsic p-type narrow band gap semiconductor,[24–28] crystallizes in a cubic rock salt structure (space group $Fm\bar{3}m$) with disordered Ag and Sb positions.[29] Apart from possessing a low thermal conductivity like other members, $AgSbSe_2$ has a favorable valence band structure that consists of 12 half-pockets located at the *X*-point of the Brillouin zone.[30,31]

Although $AgSbSe_2$ has a favorable valence band structure, the electrical conductivity of the pristine sample is low, which results in a poor thermoelectric performance.[24] Density functional theory based calculations on $AgSbSe_2$ by Mahanti and coworkers indicated that the strongly hybridized state of Sb p and that of Se shows a significant contribution near the Fermi level in the density of states (DOS) of $AgSbSe_2$.[30] Thus, in order to improve the electrical conductivity of $AgSbSe_2$, either a divalent (Pb^{2+}, Cd^{2+}, Zn^{2+}, Sn^{2+}) or monovalent cation (Na^{+}) were earlier doped into the Sb site.[24–28] Divalent (M^{2+}) and monovalent (M^{+}) cation dope the Sb^{3+} sublattice, and from simple valence counting, contribute one and two extra p-type carrier(s), respectively (Table 1), thus enhancing the carrier concentration and electrical conductivity of $AgSbSe_2$. If one can create an Sb deficiency (*i.e.* $AgSb_{1-x}Se_2$), then three extra p-type carriers can be generated per Sb deficiency (Table 1), which will possibly enhance the electrical conductivity without the addition of any foreign dopant. Although the effect of doping various cations on the thermoelectric properties of $AgSbSe_2$ has been extensively studied, an investigation into the effect of nonstoichiometry or cation deficiency has not been carried out to date.

Herein, we report the effect of Sb deficiency [$AgSb_{1-x}Se_2$; x = 0–3 mol%] on the thermoelectric properties of p-type $AgSbSe_2$ for the first time. We have shown that the hole transport in $AgSbSe_2$ can be significantly tuned by controlling the Sb stoichiometry without the addition of any foreign dopant. The p orbital of Sb shows a significant contribution near the Fermi level in the DOS of $AgSbSe_2$,[30] and thus creation of Sb deficiencies can result in tuning of the Fermi level. Our experimental results demonstrate that a small amount of Sb deficiencies markedly increases the hole concentrations, which indeed enhances the electrical conductivity up to $\sim$90 S cm^{-1} from 4.5 S cm^{-1} (for the pristine sample) at room temperature. Although there is a slight decrease in the Seebeck coefficient for Sb deficient samples, the large increase in σ results in an improved power factor ($S^2\sigma$) over a wide temperature range (300–620 K). With this enhanced power factor and ultra-low thermal conductivity ($\sim$0.4 W m^{-1} K^{-1}), a maximum ZT of $\sim$1 at 610 K has been achieved in the $AgSb_{0.9925}Se_2$ and $AgSb_{0.9925}Se_2$ samples. A maximum theoretical thermoelectric efficiency (η_{max}) of $\sim$8% was calculated by considering a virtual thermoelectric module consisting of the present p-type $AgSb_{1-x}Se_2$ and previously reported n-type $AgBiSe_2$,[20b] by maintaining the temperature difference of ΔT = 400 K.

Table 1 From simple valence calculation, number(s) of hole(s) expected for per cation substitution or deficiency in the Sb^{3+} position in $AgSbSe_2$

Sample	Number of expected holes per substitution in the Sb position
$AgSb_{1-x}M_xSe_2$ (M^{2+} = divalent cation; x = mol%)	1
$AgSb_{1-x}M_xSe_2$ (M^{+} = monovalent cation; x = mol%)	2
$AgSb_{1-x}Se_2$ (Sb^{3+} trivalent cation deficiency; x = mol%)	3

2. Experimental section

2.1 Elements

Elemental silver (Ag, 99.9999%, metal basis), elemental antimony (Sb, 99.9999%, metal basis), and elemental selenium (Se, 99.999%, metal basis) were purchased from Alfa Aesar and used for synthesis without further purification.

2.2 Synthesis

Ingots ($\sim$7 g) of $AgSb_{1-x}Se_2$ (x = 0–3 mol%) were synthesized by mixing appropriate ratios of high-purity Ag, Sb and Se in quartz tubes. The tubes were flame sealed under a high vacuum ($\sim 10^{-5}$ Torr) and slowly heated up to 673 K over 12 h, then heated up to 1123 K in 4 h, soaked for 10 h, and subsequently air quenched to room temperature. The air quenched samples were then annealed at 600 K for 10 h. For electrical and thermal transport measurements the samples were cut and polished using a diamond saw. Bar-shaped samples were used for simultaneous electrical conductivity and Seebeck coefficient measurements, whereas coin-shaped samples were used for thermal transport measurements.

2.3 Powder X-ray diffraction

Powder X-ray diffraction for all the as synthesized samples were recorded using a Cu K_α (λ = 1.5406 Å) radiation source on a Bruker D8 diffractometer.

2.4 Field emission scanning electron microscopy (FESEM)-back-scattered electron (BSE) imaging

An FESEM-BSE imaging experiment was performed using NOVA NANO SEM 600 (FEI, Germany) operated at 15 kV.

2.5 Band gap

To probe the room temperature optical band gap, optical diffuse reflectance measurements were performed on finely ground powder samples. The spectra were recorded over the range of 600 nm to 2500 nm using a Perkin Elmer Lambda 900, UV/Vis/NIR spectrometer. Absorption (α/S) data were calculated from reflectance data using Kubelka–Munk equations: $\alpha/S = (1 - R)^2/(2R)$, where R is the reflectance and α and S are the absorption and scattering coefficients, respectively.

2.6 Carrier concentration

Room temperature carrier concentration has been derived from Hall coefficient measurements using a PPMS (Physical Property Measurement System, Quantum Design, USA).

2.7 Electrical transport

Electrical conductivity and Seebeck coefficients were measured simultaneously under a helium atmosphere from room temperature to ~623 K on a ULVAC RIKO ZEM-3 instrument system. The typical sample for the measurement has a rectangular shape with the dimensions of ~2 mm × 2 mm × 8 mm. The longer direction coincides with the direction in which the thermal conductivity was measured. Heating and cooling cycles give repeatable electrical properties for a given sample (ESI,† Fig. S4).

2.8 Thermal transport

A Netzsch LFA-457 laser flash was used for thermal diffusivity, D, measurements from room temperature to ~623 K under a N_2 atmosphere (Fig. S1, ESI†). Coins of ~8 mm diameter and ~2 mm thickness were used for the measurements. The samples were coated with a thin layer of graphite to minimize errors from the emissivity of the material. Temperature dependent heat capacity, C_p, was derived using standard sample (pyroceram) in LFA457 (Fig. S1, ESI†). The thermal diffusivity data were analyzed using a Cowan model with pulse correction. The total thermal conductivity, κ_{total}, was calculated using the formula, $\kappa_{total} = DC_p\rho$, where ρ is the density of the sample, measured using sample dimension and mass. The density of the pellets obtained was in the range of ~97% of the theoretical density.

2.9 Thermoelectric efficiency (η) calculations

The overall thermoelectric figure of merit of a p and n-type pair [$(ZT)_m$] of thermoelectric materials was theoretically calculated from eqn (1)[32]

$$(ZT)_m = \int_{T_C}^{T_H} \frac{(S_p - S_n)^2 \cdot T}{\left[\sqrt{\rho_p \cdot \kappa_p} + \sqrt{\rho_n \cdot \kappa_n}\right]^2 \cdot \Delta T} dT \qquad (1)$$

where, (S_p and S_n), (ρ_p and ρ_n) and (κ_p and κ_n) represent the Seebeck coefficient, electrical resistivity and total thermal conductivity of p-and n-type materials, respectively. The theoretical conversion efficiency of the aforementioned pair of materials was calculated from eqn (2)[32]

$$\eta = \frac{\Delta T}{T_H} \frac{\sqrt{1 + (ZT)_{m,avg}} - 1}{\sqrt{1 + (ZT)_{m,avg}} + \frac{T_C}{T_H}} \qquad (2)$$

where $\Delta T/T_H$ refers to the Carnot efficiency, T_H and T_C are the hot and cold side temperatures and $(ZT)_{m,avg}$ is the average figure-of-merit of a pair of thermoelectric legs.

3. Results and discussion

3.1 Structural and optical characterizations

Powder X-ray diffraction (XRD) patterns of pristine $AgSbSe_2$ and non-stoichiometric [$AgSb_{1-x}Se_2$ (x = 0.5–3 mol%)] samples have been presented in Fig. 1a. In all the cases, PXRD patterns could be index based on cubic $AgSbSe_2$ (space group $Fm\bar{3}m$). No impurity peaks were observed within the detection limit of the PXRD, which indicates that Sb deficiency in the sample does not create any new second phase. For further confirmation, we have performed field emission scanning electron microscopy (FESEM) *via* back-scattered electron (BSE) imaging of the $AgSb_{0.9925}Se_2$ sample (see Fig. 1b). The BSE image is uniform and shows no contrast difference, which confirms the absence of second phase segregation.

The optical absorption spectra of the selected samples are shown in Fig. 1c. Measured band gaps for all the Sb deficient samples are slightly higher than that of pristine $AgSbSe_2$. We observed an increase in the p-type carrier concentration with increasing the concentration of Sb deficiencies (see the later part of the paper), which indicates the shift of the Fermi level to deeper inside the valence band. Moving of the Fermi level inside the valence band probably gives rise to a slight increase in the band gap for Sb deficient samples.

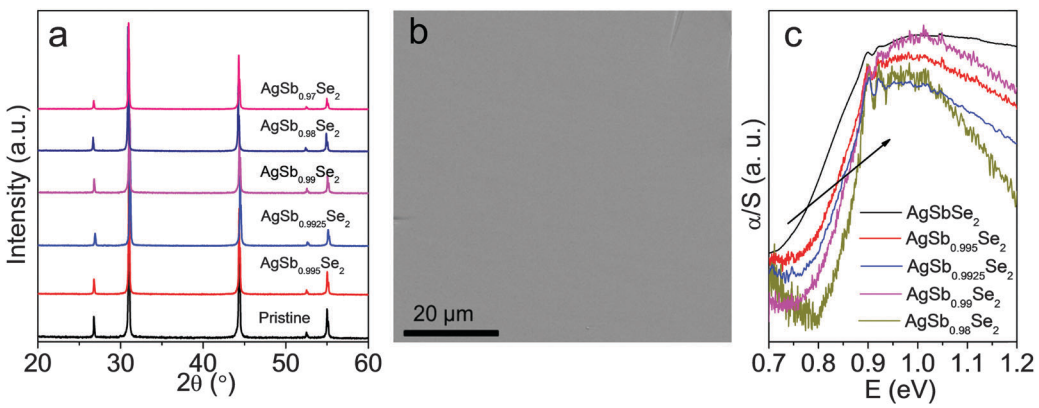

Fig. 1 (a) Powder XRD patterns (b) FESEM-backscattered electron (BSE) image of $AgSb_{0.9925}Se_2$ sample and (c) optical absorption spectra of $AgSb_{1-x}Se_2$ (x = 0–2 mol%) at room temperature.

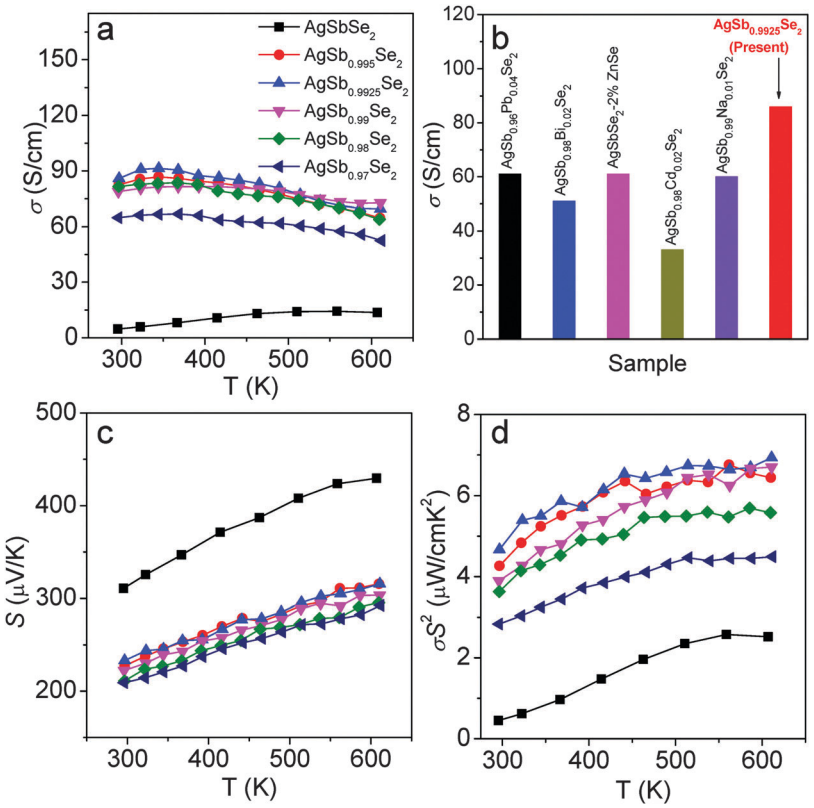

Fig. 2 (a) Temperature dependent electrical conductivity (σ) of $AgSb_{1-x}Se_2$ (x = 0–3 mol%) samples. (b) Room temperature σ of $AgSb_{0.9925}Se_2$ compared with that of different cation doped $AgSbSe_2$;[24–28] Temperature dependent (c) Seebeck coefficient (S) and (d) power factor (σS^2) of $AgSb_{1-x}Se_2$ (x = 0–3 mol%) samples.

Table 2 Room temperature carrier concentration (n_h), carrier mobility (μ) and effective mass (m^*) of selected $AgSb_{1-x}Se_2$ (x = 0–3 mol%) samples

Sample	n_h (cm^{-3})	μ (cm^2 V^{-1} s^{-1})	m^*/m_0
$AgSbSe_2$	5×10^{18}	7	1.2
$AgSb_{0.9925}Se_2$	1.98×10^{19}	17	1.46
$AgSb_{0.99}Se_2$	2.8×10^{19}	17.5	1.68
$AgSb_{0.97}Se_2$	6.93×10^{19}	5.8	2.74

3.2 Electrical transport properties

Temperature dependent electrical conductivity (σ) of pristine and Sb deficient samples are presented in Fig. 2a. We have observed a large increase in the σ value in all the Sb deficient samples compared to that of pristine $AgSbSe_2$. σ shows a weak temperature dependence with increase of temperature. The highest room temperature σ is to be $\sim$86 S cm^{-1} for $AgSb_{0.9925}Se_2$, which reaches a value of $\sim$70 S cm^{-1} at 610 K.

We have estimated the room temperature carrier concentration, n_h, from the equation: $n_h = 1/eR_H$, where R_H is the Hall coefficient, e is the electronic charge. The carrier mobility (μ) was calculated using the formula, $\mu = \sigma/n_h e$. The measured carrier concentration and carrier mobility for selected samples are presented in Table 2. Sb deficient samples show significantly higher hole concentrations (n_h) compared to that of the pristine sample.

The Sb deficient samples show higher σ values compared to those of previously reported divalent (M^{2+} = Pb^{2+}, Zn^{2+}, Cd^{2+}) or monovalent (M^+ = Na^+) cation doped $AgSbSe_2$ (Fig. 2b).[24–28] When a divalent M^{2+} cation is substituted in the Sb^{3+} position, then for each substitution it contributes one extra hole (Table 1), which is calculated from the simple valence counting chemistry. Similarly, for monovalent M^+ cation doping, each substitution in place of Sb^{3+} contributes two extra holes (Table 1). In the present case, each Sb vacancy gives rise to three extra holes as Sb is trivalent (Table 1), thus the required Sb deficiency concentration is three times less compared to the doping concentration of the M^{2+} cation. For, example, optimized doping concentration for Zn^{2+}/Cd^{2+} in $AgSbSe_2$ was 2 mol%,[25,26] whereas optimized Sb deficiency concentration is 0.75 mol% which is approximately three times less than M^{2+} doping concentration. Notably, Sb deficient samples show higher carrier mobility compared to the cation doped samples,[24–26] which is probably due to the absence of a foreign dopant in the present $AgSb_{1-x}Se_2$ samples.

In Fig. 2c, we represent temperature dependent Seebeck coefficient (S) of $AgSb_{1-x}Se_2$ (x = 0–3 mol%) samples. The positive sign of S indicates p-type conduction in all the samples, which agrees well with the Hall coefficient data. All the Sb deficient samples show slightly lower Seebeck values compared to that of the pristine sample, which is due to higher carrier concentration of Sb deficient samples compared to that of pristine $AgSbSe_2$. Typically, the $AgSb_{0.9925}Se_2$ samples show an S value of $\sim$233 μV K^{-1} at room temperature, which increases

with the increasing the temperature and reaches a value of ~316 μV K^{-1} at 610 K. We have estimated effective mass (m^*) of the carriers in $AgSb_{1-x}Se_2$ (x = 0–3 mol%) using measured S and Hall carrier concentration (n_h) at room temperature (Table 2).[24] Although accurate calculation of m^* requires consideration of the non-parabolic band and multiple band model, the present calculation of m^* considers only single parabolic band for simplicity. Increased population of carriers in the multiple flat valence band valleys of the Sb deficient sample produces high m^* in $AgSb_{1-x}Se_2$ samples (Table 2). The calculated m^* values are comparable to the previously reported value for the divalent and monovalent cation doped $AgSbSe_2$.[24–28]

From the measured σ and S, we have estimated the temperature dependent power factors (σS^2) for all the samples (Fig. 2d). A maximum σS^2 of ~2.5 μW cm^{-1} K^{-2} at ~608 K was achieved for the pristine $AgSbSe_2$ sample. The combination of improved σ and moderate Seebeck coefficient resulted in an enhancement in the σS^2 value for all the Sb deficient samples. Typically, the $AgSb_{0.9925}Se_2$ sample shows a σS^2 value of ~4.7 μW cm^{-1} K^{-2} at room temperature which reaches a value of ~6.94 μW cm^{-1} K^{-2} at 610 K. All the Sb deficient samples show reasonably constant power factors over the measured temperature.

3.3 Thermal transport properties

The temperature dependent thermal conductivities of all $AgSb_{1-x}Se_2$ (x = 0–3 mol%) samples are presented in Fig. 3. Temperature dependent total thermal conductivity, κ_{total}, (Fig. 3a) values of $AgSb_{1-x}Se_2$ (x = 0–3 mol%) samples were estimated over the 300–623 K temperature range using the formula, $\kappa_{total} = DC_p\rho$, where D is thermal diffusivity, C_p is specific heat and ρ is the density of the sample (ESI,† Fig. S1). All the samples show ultra-low thermal conductivity in the 300–623 K temperature range. At room temperature a κ_{total} value of ~0.44 W m^{-1} K^{-1} was measured for $AgSb_{0.9925}Se_2$, which remains nearly constant throughout the measured temperature range. Temperature dependent lattice thermal conductivity, κ_{lat}, values were obtained by subtracting the electronic thermal conductivity, κ_{ele}, from the κ_{total}. The κ_{ele} were estimated using the Wiedemann–Franz law, $\kappa_{ele} = L\cdot\sigma\cdot T$; where, L is Lorenz number, σ is electrical conductivity and T is temperature. Temperature dependent L values were extracted based on the fitting of the respective temperature dependent S values (ESI,† Fig. S2) that estimate the reduced chemical potential, which was elaborated elsewhere.[24] The κ_{ele} of all the samples are presented in Fig. S3 (ESI†). The κ_{lat} value for the $AgSb_{0.9925}Se_2$ sample at room temperature is ~0.40 W m^{-1} K^{-1}, which remains nearly constant throughout measured temperature range. Similar κ_{lat} values were previously reported in the case of cation doped $AgSbSe_2$.[24–28] Highly anharmonic Sb–Se bonds and disordered cation sublattice contribute to phonon scattering processes, which give rise to low κ_{lat} in $AgSb_{1-x}Se_2$.

In order to find out the contribution of κ_{lat} in κ_{total}, we have calculated the ratio of κ_{lat} and κ_{total} as a function of temperature for the pristine and $AgSb_{0.9925}Se_2$ sample (Fig. 3c). The major portion of heat conduction in the pristine sample takes place through phonon transport, because of low electrical

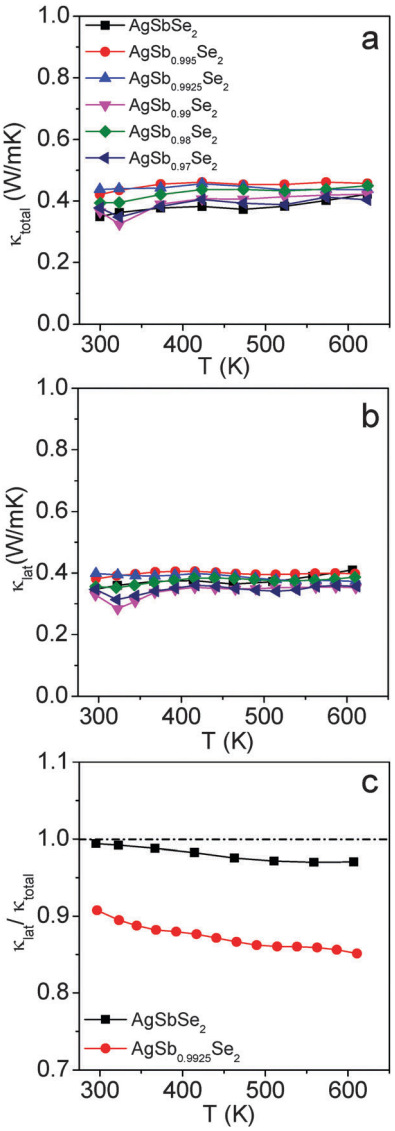

Fig. 3 Temperature dependent (a) total thermal conductivity (κ_{total}) and (b) lattice thermal conductivity (κ_{lat}) of $AgSb_{1-x}Se_2$ (x = 0–3 mol%) samples. (c) Temperature dependent $\kappa_{lat}/\kappa_{total}$ of $AgSbSe_2$ and $AgSb_{0.9925}Se_2$ samples.

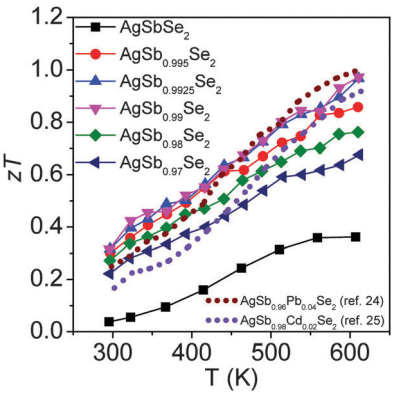

Fig. 4 Temperature dependent thermoelectric figure merit (ZT) of $AgSb_{1-x}Se_2$ (x = 0–3 mol%) samples compared with previously reported Pb and Cd doped $AgSbSe_2$ (dotted line).[24,25]

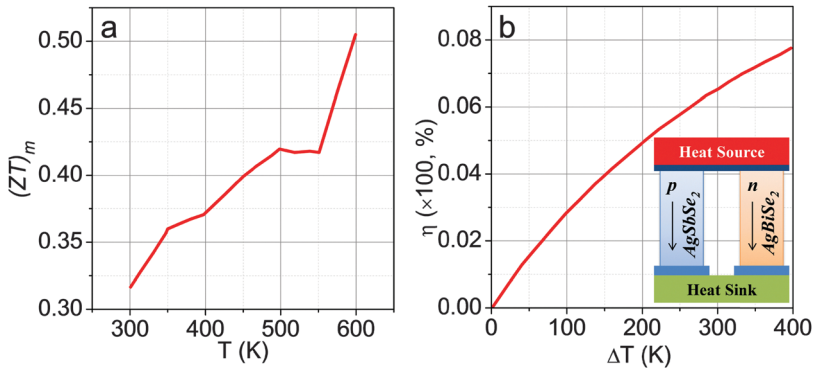

Fig. 5 (a) The overall theoretical thermoelectric figure of merit [$(ZT)_m$] of a p and n-type pair, considering present $AgSb_{0.9925}Se_2$ as p-type leg and previously reported $AgBiSe_{1.98}Cl_{0.02}$ as n-type leg. (b) Theoretical thermoelectric energy conversion efficiency (η) as a function of temperature difference (ΔT) for thermoelectric devices considering $AgSb_{0.9925}Se_2$ and $AgBiSe_{1.98}Cl_{0.02}$[20b] as p-type and n-type material, respectively. Inset in panel (b) represent schematic of a typical thermoelectric module.

conductivity. However, for the $AgSb_{0.9925}Se_2$ sample, the phonon contribution to the total thermal conductivity is ~90% in the 300–610 K temperature range, even though there was a significant increase in electrical conductivity. Thus, κ_{total} in the $AgSbSe_2$ system is intrinsically dominated by heat conduction through lattice vibrations.

3.4 Thermoelectric figure of merit

Temperature dependent thermoelectric figure of merits (ZT) of all $AgSb_{1-x}Se_2$ (x = 0–3 mol%) samples are estimated from the measured electrical and thermal transport data. In Fig. 4 we present the ZT values of $AgSb_{1-x}Se_2$ (x = 0–3 mol%) samples. We also compare the present ZT *vs.* T data with those of the previously reported high performance Pb and Cd doped $AgSbSe_2$ samples (dotted lines in Fig. 4).[24,25] The highest ZT value measured in the present case is indeed comparable to that of the monovalent or divalent cation doped $AgSbSe_2$.[24–28] Enhanced electrical transport due to Sb deficiencies and ultra-low thermal conductivity due to bond anharmonicity and disordered cation sublattice resulted in a superior performance in Sb deficient samples compared to pristine $AgSbSe_2$. The maximum ZT ~ 1 at 610 K was achieved for both the $AgSb_{0.9925}Se_2$ and $AgSb_{0.99}Se_2$ samples without the use of any foreign dopant. Notably, we have achieved ~170% improvement in ZT in Sb deficient sample compared to that of pristine $AgSbSe_2$.

3.5 Thermoelectric conversion efficiency (η)

The overall thermoelectric figure of merit of a p and n-type pair, $[(ZT)_m]$, was theoretically calculated using eqn (1) (see Experimental section), considering the present $AgSb_{0.9925}Se_2$ and previously reported $AgBiSe_{1.98}Cl_{0.02}$ as p-type and n-type materials, respectively (Fig. 5a). We have chosen $AgBiSe_{1.98}Cl_{0.02}$ as n-type, as this material is also belongs to the I–V–VI_2 class.[20b] A maximum $(ZT)_m$ value of 0.53 at 600 K was calculated for the above mentioned theoretical module. To calculate the theoretical efficiency (η) of this pair, first we have calculated the $(ZT)_{m,avg}$ from the $(ZT)_m$ considering a hot side temperature of 600 K and cold side temperature of 300 K. A $(ZT)_{m,avg}$ of ~0.45 was estimated. A maximum conversion efficiency (η_{max}) of ~8% was calculated theoretically by fixing the cold side temperature to 300 K by maintaining a temperature difference of ΔT = 400 K (Fig. 5b). The present theoretical η_{max} value is comparable to that of the market based metal telluride thermoelectric generator for mid-temperature applications.

4. Conclusions

In conclusion, we have demonstrated a new way to control the p-type carrier concentrations in high quality crystalline ingots of $AgSbSe_2$ without the addition of any foreign dopant. We have shown that Sb deficiency can play a crucial role in tuning the electronic transport properties of $AgSbSe_2$. From simple valence counting, each Sb deficiency creates three extra holes in $AgSbSe_2$, which results in an improved carrier concentration, thus giving rise to enhanced electronic conductivity. The combination of improved electrical conductivity and reasonable Seebeck coefficient leads to high and constant power factor values in the 300–610 K temperature range. A highly anharmonic Sb–Se bond and disordered Ag/Sb sublattice significantly scatter the heat carrying phonons, thus resulting in ultra-low κ_{lat}. Improved electronic transport and low thermal conductivity provided a maximum ZT value of ~1 at 610 K for both the Sb deficient $AgSb_{0.9925}Se_2$ and $AgSb_{0.99}Se_2$ samples. A maximum thermoelectric conversion efficiency (η_{max}) of ~8% was estimated theoretically by considering $AgSb_{1-x}Se_2$ and $AgBiSe_{2-x}Cl_x$ as p-type and n-type materials, respectively, which shows the potential for the use of this class of materials in mid-temperature power generation applications.

Acknowledgements

This work was supported through a DST Ramanujan Fellowship, the New Chemistry Unit and Sheikh Saqr Laboratory, JNCASR. S.N.G. thanks JNCASR for a research fellowship. We thank Mr Somnath Ghara for his help during Hall measurements. The authors also thank Dr Suresh Perumal for his help with the conversion efficiency calculations.

References

1 L.-D. Zhao, V. P. Dravid and M. G. Kanatzidis, *Energy Environ. Sci.*, 2014, **7**, 251–268.
2 G. J. Snyder and E. S. Toberer, *Nat. Mater.*, 2008, **7**, 105–114.
3 J. Sootsman, D. Y. Chung and M. G. Kanatzidis, *Angew. Chem., Int. Ed.*, 2009, **48**, 8616–8639.
4 M. Zebarjadi, K. Esfarjani, M. S. Dresselhaus, Z. F. Ren and G. Chen, *Energy Environ. Sci.*, 2012, **5**, 5147–5162.
5 K. Biswas, J. He, I. D. Blum, C. I. Wu, T. P. Hogan, D. N. Seidman, V. P. Dravid and M. G. Kanatzidis, *Nature*, 2012, **489**, 414–418.
6 L.-D. Zhao, S.-H. Lo, Y. Zhang, H. Sun, G. Tan, C. Uher, C. Wolverton, V. P. Dravid and M. G. Kanatzidis, *Nature*, 2014, **508**, 373–377.
7 J. P. Heremans, V. Jovovic, E. S. Toberer, A. Saramat, K. Kurosaki, A. Charoenphakdee, S. Yamanaka and G. J. Snyder, *Science*, 2008, **321**, 554–557.
8 (*a*) Q. Zhang, B. Liao, Y. Lan, K. Lukas, W. Liu, K. Esfarjani, C. Opeil, D. Broido, G. Chen and Z. Ren, *Proc. Natl. Acad. Sci. U. S. A.*, 2013, **110**, 13261–13266; (*b*) A. Banik and K. Biswas, *J. Mater. Chem. A*, 2014, **2**, 9620–9625.
9 Y. Pei, X. Shi, A. La Londe, H. Wang, L. Chen and G. J. Snyder, *Nature*, 2011, **473**, 66–69.
10 (*a*) W. Liu, X. Tan, K. Yin, H. Liu, X. Tang, J. Shi, Q. Zhang and C. Uher, *Phys. Rev. Lett.*, 2012, **108**, 166601; (*b*) A. Banik, U. S. Shenoy, S. Anand, U. V. Waghmare and K. Biswas, *Chem. Mater.*, 2015, **27**, 581–587.
11 T. C. Harman, P. J. Taylor, M. P. Walsh and B. E. LaForge, *Science*, 2002, **297**, 2229–2232.
12 L. D. Hicks and M. S. Dresselhaus, *Phys. Rev. B: Condens. Matter Mater. Phys.*, 1993, **47**, 12727.
13 Y. Sun, H. Cheng, S. Gao, Q. Liu, Z. Sun, C. Xiao, C. Wu, S. Wei and Y. Xie, *J. Am. Chem. Soc.*, 2012, **134**, 20294–20297.
14 J. P. Heremans, C. M. Thrush and D. T. Morelli, *Phys. Rev. B: Condens. Matter Mater. Phys.*, 2004, **70**, 115334.
15 M. G. Kanatzidis, *Chem. Mater.*, 2010, **22**, 648–659.
16 K. Biswas, J. He, Q. Zhang, G. Wang, C. Uher, V. P. Dravid and M. G. Kanatzidis, *Nat. Chem.*, 2011, **3**, 160–166.
17 K. F. Hsu, S. Loo, F. Guo, W. Chen, J. S. Dyck, C. Uher, T. Hogan, E. K. Polychroniadis and M. G. Kanatzidis, *Science*, 2004, **303**, 818–821.
18 B. Poudel, Q. Hao, Y. Ma, Y. Lan, A. Minnich, B. Yu, X. Yan, D. Wang, A. Muto, D. Vashaee, X. Chen, J. Liu, M. S. Dresselhaus, G. Chen and Z. Ren, *Science*, 2008, **320**, 634–638.
19 (*a*) Y. He, T. Day, T. Zhang, H. Liu, X. Shi, L. Chen and G. J. Snyder, *Adv. Mater.*, 2014, **26**, 3974–3978; (*b*) H. Liu, X. Shi, F. Xu, L. Zhang, W. Zhang, L. Chen, Q. Li, C. Uher, T. Day and G. J. Snyder, *Nat. Mater.*, 2012, **11**, 422–425.
20 (*a*) L. Pan, D. Berardan and N. Dragoe, *J. Am. Chem. Soc.*, 2013, **135**, 4914–4917; (*b*) S. N. Guin, V. Srihari and K. Biswas, *J. Mater. Chem. A*, 2015, **3**, 648–655; (*c*) C. Xiao, X. Qin, J. Zhang, R. An, J. Xu, K. Li, B. Cao, J. Yang, B. Ye and Y. Xie, *J. Am. Chem. Soc.*, 2012, **134**, 18460–18466.
21 (*a*) S. N. Guin, J. Pan, A. Bhowmik, D. Sanyal, U. V. Waghmare and K. Biswas, *J. Am. Chem. Soc.*, 2014, **136**, 12712–12720; (*b*) S. Lee, K. Esfarjani, T. Luo, J. Zhou, Z. Tian and G. Chen, *Nat. Commun.*, 2014, **5**, 3525.
22 (*a*) M. D. Nielsen, V. Ozolins and J. P. Heremans, *Energy Environ. Sci.*, 2013, **6**, 570–578; (*b*) F. D. Rosi, E. F. Hockings and N. E. Lindenblad, *RCA Rev.*, 1961, **22**, 82–121; (*c*) S. N. Guin and K. Biswas, *Chem. Mater.*, 2013, **25**, 3225–3231.
23 D. T. Morelli, V. Jovovic and J. P. Heremans, *Phys. Rev. Lett.*, 2008, **101**, 035901.
24 S. N. Guin, A. Chatterjee, D. S. Negi, R. Datta and K. Biswas, *Energy Environ. Sci.*, 2013, **6**, 2603–2608.
25 S. N. Guin, A. Chatterjee and K. Biswas, *RSC Adv.*, 2014, **4**, 11811–11815.
26 S. N. Guin, D. S. Negi, R. Datta and K. Biswas, *J. Mater. Chem. A*, 2014, **2**, 4324–4331.
27 S. Cai, Z. Liu, J. Sun, R. Li, W. Fei and J. Sui, *Dalton Trans.*, 2015, **44**, 1046–1051.
28 D. Li, X. Y. Qin, T. H. Zou, J. Zhang, B. J. Ren, C. J. Song, Y. F. Liu, L. Wang, H. X. Xin and J. C. Li, *J. Alloys Compd.*, 2015, **635**, 87–91.
29 S. Geller and J. H. Wernick, *Acta Crystallogr.*, 1959, **12**, 46–54.
30 K. Hoang, S. D. Mahanti, J. R. Salvador and M. G. Kanatzidis, *Phys. Rev. Lett.*, 2007, **99**, 156403.
31 (*a*) K. Wojciechowski, M. Schmidt, J. Tobola, M. Koza, A. Olech and R. Zybaia, *J. Electron. Mater.*, 2010, **39**, 2053–2058; (*b*) K. T. Wojciechowski and M. Schmidt, *Phys. Rev. B: Condens. Matter Mater. Phys.*, 2009, **79**, 184202.
32 D. M. Rowe, *CRC handbook of thermoelectrics*, CRC Press, Boca Raton, FL, 1995.